1966

Charged Particle Fluxes In The South Atlantic Radiation Anomaly

Nicholas S. P. King

CHARGED PARTICLE FLUXES IN THE SOUTH ATLANTIC RADIATION ANOMALY

By

Nicholas S. P. King

A Thesis

Submitted in Partial Fulfillment

of the Requirements for the Degree of

Master of Science in Physics

The University of New Mexico
1966

This thesis, directed and approved by the candidate's committee, has been accepted by the Graduate Committee of the University of New Mexico in partial fulfillment of the requirements for the degree of

MASTER
OF
SCIENCE

Art Steger
Dean

Date 6-6-66

CHARGED PARTICLE FLUXES IN THE SOUTH ATLANTIC RADIATION ANOMALY

Nicholas S. P. King

Thesis committee

A. P. Leavitt
Chairman

Roy Thoms

Gustav A. Pegues

Table of Contents

ABSTRACT

Data from a scintillator and two Cerenkov counters aboard the OSO-B2 satellite are converted from counting rates to omnidirectional fluxes in the South Atlantic Radiation Anomaly. Isointensity contours are obtained for the anomaly with omnidirectional fluxes being of the order of 90 protons/cm^2-sec and 5×10^3 electrons/cm^2-sec. The South Atlantic Radiation Anomaly is postulated to include an electron dump into the earth's atmosphere due to the observed differences between the isointensity distributions for protons and electrons.

ACKNOWLEDGEMENTS

I would like to express my appreciation to Dr. C. P. Leavitt for his invaluable assistance and guidance in the preparation of this thesis. I would also like to thank Mr. Pete Horney for his assistance in data reduction.

Introduction

In 1959, Dessler (Dessler, 1959) indicated that the existence of anomalies in the surface magnetic field of the earth could cause large perturbations from the average trapped radiation belt distribution above the surface. Such an anomaly is found in the South Atlantic Ocean centered approximately at 45 degrees south latitude, 28 degrees west longitude. Contours of constant magnetic field intensity at the earth's surface as compiled by Cain et al (Cain, 1965) is shown in Figure 1. Yoshida et al (Yoshida, 1960) concluded that as a result of this anomaly the inner radiation belt over the South Atlantic would dip to much lower than average altitudes.

A considerable number of rocket and satellite experiments since then have verified the existence of a South Atlantic radiation anomaly (SARA) at altitudes above 300 kilometers. These experiments have revealed considerably higher proton and electron fluxes than are found in the immediate neighborhood of SARA at low altitudes (less than 1000 km). The results of one of these experiments (Freden and Paulikas, 1964) are shown in Figure 2 for a satellite altitude of 600 km and at proton energies of 5 to 20 Mev.

A simple model for SARA is one in which geomagnetic field lines form mirror planes for charged particles.

The fact that the magnetic field intensity is weaker in the anomaly region permits charged particles to reach lower altitudes before being mirrored than in other regions. An experiment by Heckman and Nakano (Heckman and Nakano, 1963) has located a preferred region for such mirroring. Figure 3 shows the projection of this region onto the earth's surface.

Since the field lines in the anomaly are a perturbation on those in the earth's inner radiation belt one should expect a particle composition similar to those found there. This radiation belt is characterized by large trapped proton fluxes (>100 protons/cm^2-sec) with only slight variations in time. The South Atlantic Anomaly also seems to have the above characteristics which gives some justification for the mirror model. As yet, a completely satisfactory model for low altitude radiation anomalies has not been found which can adequately describe its origins or injection mechanisms for particles into the anomalies. An injection mechanism is found necessary to account for stability as the anomaly apparently acts as a charged particle dump into the atmosphere.

The Experiment

Integrated proton and electron fluxes for energies greater than 1 to 2 Mev were measured over a period of six months from February 3, 1965 to July 15, 1965 from the NASA Orbiting Solar Observatory B-2 (OSO-B2). Out of 2411 orbits

approximately 804 passed with 80 degrees east longitude and 40 degrees west longitude giving 427 hours of data in the South Atlantic Radiation Anomaly. Not all of the data has been reduced or was used in this analysis.

OSO-B2 carried a number of experiments located both in sail and spinning wheel sections. This experiment was located in one of the nine wheel compartments (Figures 4 and 5).

The primary purpose of the UNM OSO-B2 experiment was to measure the direction of arrival and energies of primary cosmic ray gamma rays over an energy range of 100 to 1000 Mev.

The gamma ray telescope was designed to give an energy resolution of 20 to 30% with directional accuracies of ± 10 degrees. Unfortunately, due to reasons not entirely established, the telescope flux proved to be too high by a factor of 1000 from the expected 10^{-4} gammas per cm^2-sec. Dr. C. P. Leavitt, the cognizant physicist for this experiment, has suggested that a failure of the charged particle anticoincidence counter due to a threshold drift is possible.

This experiment is the reduction and analysis of charged particle counting rates obtained over SARA from the three components of the gamma ray telescope. As the telescope was not specifically designed for this secondary experiment the individual counter efficiencies and geometric factors can only

roughly estimated.

The Satellite

The OSO-B2 satellite was launched from the Cape Kennedy NASA installation on February 3, 1965 with a payload of 545 lbs of which approximately 207 lbs were due to experiments. The pertinent orbit parameters are given in Table I and a typical orbit passing through the anomaly is shown in Figure 6.

Table I

Perigee Apogee (km)	Inclination	Period	Eccentricity	Precession per Orbit
553 633	33°	96 min.	.00574	25°W

The spacecraft was designed to serve as a stabilized platform for solar oriented experiments. Experiments not requiring a fixed solar orientation were housed in the spinning wheel. The wheel is 44 in. in diameter and 8 in. high affording each experiment an 1/8-inch aluminum walled compartment 1000 cubic inches in volume. The average spin rate is .528 rev/sec with the satellite oriented so that each experiment in the wheel sees the sun every 2 seconds. The sail is oriented towards the solar center within ± 1 minute of arc by a system of roll and pitch gas jets (Figure 7). Spin gas jets maintain the wheel spin rate so that through gyroscopic action the roll rate is very low. The orientation

of the sail plane towards the sun will enhance the probability that the wheel plane will not spin in the assumed mirror planes of SARA. This enhancement, as well as the low probability for spinning in the mirror planes for random orientations of the spin axis in space justifies the assumption that, for geometric calculations, the wheel can be assumed to spin out of the mirror planes.

Satellite data is tape recorded in a time-multiplexed system of 32 main frame words of 8 bits each at a real data time rate of 400 bits per second (bps) or .64 seconds per frame.

Playback of the satellite tape is initiated once per orbit at a rate of 7200 bps requiring approximately 5.5 min. to complete one orbit's data. During this playback time no data is recorded by the satellite.

The UNM experiment was allocated two main frame channels plus three channels in a two main frame subcommutated wheel channel. The two main frame wheel channel was subcommutated into 48 channels each of which was sampled every 15.36 seconds. Thus each of the UNM wheel channels represents an analog count rate every 15.36 seconds. The analog voltage from a ratemeter is actually recorded on a binary 8 bit register of maximum capacity $(2)^8 - 1 = 255$. This maximum value corresponds to the maximum voltage output for the specific counter as

determined from a laboratory calibration of analog voltage vs counts/sec.

The remaining wheel subcommutated channels give information concerning other experiments and spacecraft status.

The Instrument

A schematic of the gamma ray telescope is shown in Figure 8. An incident charged particle passes through a cup-shaped plastic scintillator producing a pulse which is recorded in the telemetry wheel channel number four. The scintillator cup is 2 inches in diameter and 3-1/2 inches high with an upper wall thickness of 3/8 inch and sides 1/2 inch thick. A particle can either strike the upper face or pass through the Aluminum wheel housing, the lucite light pipe, and the 1/8-inch skin of the counter before giving a pulse. The difference in the two paths is the minimum energy required of the incident particle to generate a pulse larger than the photo threshold of the photomultiplier tube. This difference can be estimated if the energy losses due to ionization and radiation for the incident particle as it traverses the Aluminum and Lucite are calculated. The range vs energy curves is given by Rossi (Rossi, 1961) for proton absorption indicate that the range of protons in air and and aluminum do not differ appreciably for energies less

than 1 Bev. Assuming that Lucite has absorption properties similar to either air or aluminum, the total absorbing thickness can be represented by the sum of twice 1.18 gm/cm^2 for aluminum and 2.28 gm/cm^2 for Lucite. Using the curve for aluminum by Rossi, the minimum energy for penetration must be greater than 65 Mev. An empirical range vs energy curve has been obtained by Katz and Penfold (Katz and Penfold, 1952) for electrons in aluminum. Inspection of energy loss/gm-cm^2 vs energy curves for electrons due to ionization losses (Evans, 1955) indicate again that Lucite will not differ in absorption properties from aluminum. The Katz and Penfold curve gives a minimum electron energy for penetration of 8.5 Mev for an absorber thickness of 4.64 gm/cm^2. For both protons and electrons it has been assumed that energy loss due to radiation in a counter is negligible. This is justified since the ratio of radiation to ionization losses becomes important only at Bev proton energies and is equal to .06 for 8 Mev electrons in aluminum.

The scintillator energy threshold was estimated by observing, on an oscilloscope, the minimum energy deposition pulse by Co^{60} electrons. The minimum pulse height was found to be 3 volts corresponding to an assumed 2.2 Mev minimum energy deposition for a loss of 1.8 Mev/gm-cm^2 at 1 to 2 Mev electron energies. The photomultiplier threshold set at .5 volts is equivalent to .35 Mev scintillator

threshold. In a discussion with Dr. Leavitt it was decided that this value is too low due to the unexplained high "gamma" count from the gamma ray telescope originating from a possible photomultiplier gain drift. That such a change has occurred is indicated by the low counting rate of the scintillator outside the anomaly and the small ratio in coincidence rates with the anticoincidence on and off. Consideration of these rates suggests a drift in threshold upward into the energy range corresponding to the passage of a minimum-ionizing particle. As a result, instead of .35 Mev the somewhat arbitrary value of 2 Mev will be assumed as the scintillator energy threshold.

The efficiency of the scintillator is unknown and will be assumed to be 100% for all energies above threshold.

The output voltage from the scintillation counter electronics as a function of input counts/sec from the photomultiplier was determined by replacing the PM tube with a variable frequency pulse generator. Rates from 235 to 30,000 counts/sec were obtained for a voltage range of .1 to 4.4 across a 10,000 ohm resistance. 10K was the assumed input impedence to the satellite binary register circuit. From the 255 maximum register value corresponding to 5.0 volts, the conversion factor for satellite readout to the calibrated voltage vs count curve is .0196 volts per register unit.

See Figure 10.

Cerenkov counters have an absolute threshold for charged particles determined by the Cerenkov process itself. These thresholds are plotted as a function of index of refraction in Figure 13. The refraction indices for Lucite and Pb-glass are 1.47 and 1.67 giving respective thresholds of 200 Kev and 140 Kev for electrons and 320 Mev and 230 Mev for protons. The proton spectrum in the anomaly from previous experiments indicates a negligible proton flux at the above energies so the Cerenkov counters serve primarily as electron counters. As a result, calculations for the Cerenkov counters will be done only for electrons.

The photomultiplier energy thresholds were determined using atmospheric mu mesons. Each of the Cerenkov counters was sandwiched between a coincidence counter pair and the coincidence Cerenkov pulse observed on an oscilloscope. Although most of the incident mu meson energy is lost due to ionization, the radiation observed on the oscilloscope via the photomultiplier arises from Cerenkov photons since the ionization produces no visible radiation in the non-scintillating Lucite or Lead Glass.

The Cerenkov threshold for mesons is given in Figure 13 as about 220 and 120 Mev for the Lucite and Lead Glass counters respectively. At these mu meson energies the

energy loss due to ionization is approximately 1.5 Mev/gm-cm^{-2} with negligible losses due to bremmstrahlung. The minimum energy deposited in the Lucite and Pb-glass is given in Table 2.

The photomultiplier thresholds were set at .52 and .6 volts with observed Lucite and Pb-glass minimum pulse heights of 1.5 and 6 volts. These values and E_{min} give energy thresholds of 6.2 and 9 Mev for the Lucite and Pb-glass Cerenkov counters. The geometry of the counters in the gamma ray telescope further increase this minimum energy threshold due to ionization losses in the material between the counters and the satellite wall. A rough estimate of these losses for electrons is given in Table 3 assuming that the contribution from bremmstrahlung losses in the counters and satellite material can be estimated from

$$\frac{\text{Rad}}{\text{Ion}} = Z \frac{T}{1600\ mc^2} \qquad \text{(Evans, 1955)}$$

where $\frac{\text{Rad}}{\text{Ion}} = 1$ for:

T = 15 Mev Pb-glass

T = 20 Mev Pb

T = 100 Mev Lucite

The efficiencies for the Cerenkov counters are again not known and it will be assumed they are 100%. Undoubtably

Table 2

	Density (gm/cm^3)	(dE/dx) ion	t (gm/cm^2)	E_{min}
Lucite	1.2	1.5	12.2	18
Pb-glass	4.08	1.5	61	91

Table 3

	Material In Path	Density (gm/cm^3)	$(dE/dx)_{ion}$	t (gm/cm^2)	E	Total E (Mev)
Lucite counter	Scint.	1	1.8	1.27	2	
	Pb	11.34	1.2	5.6	14.7	16.4
	Al	2.7	1.7	2.36	4	
	Light Pipe	1.2	1.8	2.28	6.4	12.4
	Scint.	1	1.8	1.27	2	
Pb-Glass counter	Scint.	1	1.8	1.27	2	
	Pb	11.34	1.2	5.6	26	50
	Lucite counter	1.2	1.8	12.2	22	
	Al	2.7	1.7	2.36	4	
	Lucite counter	1.2	1.8	14.4	26	30

this is incorrect since light pipe collection efficiencies depend strongly on the light pipe configurations. Presumably, however, they were designed to give better than 90% efficiency.

The conversion factors for satellite readout to the calibrated voltage vs count curves were determined in the same manner as for the scintillator. See Figures 11 and 12. The conversion factor from satellite register values to voltage is again .0196 volts per register unit.

Gain drifts in the photomultipliers can be expected if large temperature fluctuations occur in the satellite. These drifts would appreciably affect the above estimated thresholds. That this is not to be expected is shown in a typical plot of temperature variations over one orbit (Figure 9).

Geometric Considerations

In reducing the counting rate, r, of a detector to an omnidirectional flux, J(E), it becomes necessary to determine the efficiencies (e) of the counters as well as the effective areas exposed to an incident particle intensity, $I(E, \theta, \varphi)$. In this experiment it will be assumed that

$$\frac{r_i}{J(E)} = e_i g_i(E, \alpha) \qquad cm^2$$

where α is the angle between the normal to the detector area and the normal to the incident particle direction. $g(E, \alpha)$

is the geometric or area factor for the detector. The sum is taken over all exposed area components of the detector.

Before $g(E,\alpha)$ can be evaluated an incident particle intensity distribution must be assumed. This distribution will also determine the omnidirectional flux:

$$J(E) = \iint I(E,\theta,\varphi) \sin\theta \, d\theta \, d\varphi \qquad \frac{\text{particles}}{\text{cm}^2\text{-sec-Mev}}$$

The integrated counting rate is then:

$$R = \int_0^\infty \frac{r}{J(E)} f(E) \, dE \qquad \text{counts/sec}$$

where f(E) is the differential energy spectrum. The final conversion of the total integrated counting rate above a given threshold energy, J(>E), to the integrated omnidirectional flux above an energy E_o, $J(>E_o)$ is obtained from

$$G = \frac{1}{J(>E_o)} \int_{E_{th}}^\infty \frac{r}{J(E)} f(E) \, dE \qquad \text{Cm}^2$$

for

$$J(>E_o) = \int_{E_o}^\infty J(E) \, dE \qquad \text{particles/cm}^2\text{-sec}$$

Protons at 400 km in the South Atlantic Anomaly are confined very muct to a plane (Heckman and Nakano, 1963) as shown in Figure 3. As a result, the proton intensity can reasonably be assumed to be isotropic in a plane and in all planes parallel to that plane if the observed east-west flux assymmetry (Lenchek and Singer, 1962; Heckman and Nakano, 1963) is neglected. The east-west effect arises, at the point of observation, from the fact that the guiding centers for eastward moving protons are higher in altitude than for westward moving protons. Since the earth's atmospheric density is greater for lower altitudes more westward relative to eastward moving protons are absorbed.

Experimentally, at altitudes of 400 km, the effect becomes important only for protons of energy greater than 100 Mev. Therefore, in this experiment, the effect will be neglected as the earth's atmospheric density is considerably less at 600 km and the proposed differential proton energy spectrum at 600 km peaks near 25 Mev with a $1/E^2$ dependence for increasing energy. There has been no east-west effect observed for electrons.

Using a cylindrically symmetric intensity distribution with a divergence out of a particular plane of $\pm 6°$, the

geometric factor was calculated to be

$$eg(E,\alpha) = eg_{sides} + eg_{top} \qquad cm^2/degree\text{-}Mev$$

$$eg(E,\alpha) = \frac{5}{4}\frac{a}{\pi^2}\left\{4h\,K(\alpha)\cos\alpha + \pi a \sin\alpha\right\} \qquad cm^2/degree\text{-}Mev$$

α is the angle between the counter axis and the normal to the particle flux planes (See Appendix I).

Integrating eg(E,α) over a quarter wheel-revolution gives the average geometric factor per unit time for wheel rotation out of the mirror planes.

$$eg(E) = \frac{5}{2}\frac{a}{\pi^2}\left\{4hA + \pi a C\right\} \qquad cm^2/Mev$$

A and C are parameters characteristic of a particular counter.

The conversion factor G is derived in Appendix II for the Cerenkov counters.

$$G = \frac{1}{4}\,a\,E_o^{(n-1)}\left[\frac{4hA}{E_{th(s)}^{(n-1)}} + \frac{\pi a C}{E_{th(t)}^{(n-1)}}\right] \qquad cm^2$$

The omnidirectional proton flux cannot be determined until the total electron counting rate have been estimated from the Cerenkov counters.

The electron energy spectrum will be assumed to be of the form E^{-n} (n = 2) with a peak at about 600 Kev (Bloom et al., 1962). Using this energy spectrum and the experimentally observed ratio of the counting rates from the Lucite and Pb-glass Cerenkov counters, the thus far neglected contribution to the Pb-glass counting rate from electron generated bremmstrahlung photons can be estimated. One should expect a large fraction of the Pb-glass counting rate to originate from photons generated by electron interactions with the satellite material. These photons are essentially unimpeded in their paths to the Pb-glass counter where they are detected by the photon-pair production in Pb-glass-shower photon reaction. The Lucite counter will seldom produce electron pairs from incident photons because of its low atomic number.

The theoretical ratio of the counting rates from the Lucite and Pb-glass counters for an assumed incident omnidirectional electron flux is given by G_L/G_{PG} . This ratio is 2.68 for n = 2 in the electron spectrum and for no contribution from bremmstrahlung photons. The experimental ratio, including bremmstrahlung contributions is equal

to 2.98 with a standard deviation of .7. The following calculation gives an estimate of the bremmstrahlung contribution to the Pb-glass Cerenkov counter response to an incident omnidirectional electron flux.

R_{Pb} = total observed counting rate from Pb-glass counter

R_L = total observed counting rate from Lucite counter

R_{Bremms} = Bremmstrahlung contribution to pB-glass counting rate

R_{PG} = Counting rate due to electrons reaching Pb-glass counter

$$R_{Pb} = R_{Bremms} + R_{PG}$$

$$R_{Pb} = [G_{Bremms} + G_{PG}]\, J$$

$$R_L = G_L J$$

$$R_{Pb}/R_L = 2.98 \qquad G_L/G_{PG} = 2.68$$

$$G_{Bremms}/G_{PG} = 2.98\,(G_L/G_{PG}) - 1$$

$$G_{Bremms}/G_{PG} \simeq 7$$

This rough estimate of the ratio of the bremmstrahlung to direct electron geometric factors for the Pb-glass counter

indicates that about 88% of the counts observed come from bremmstrahlung photons. This also indicates why the Lucite counter response is much lower than would be anticipated from ionization threshold calculations.

Experimental Results

Isointensity contours for the Scintillation and Pb-glass counters are plotted in geographic coordinates in Figures 15 and 16. The satellite readout data was gotten from plots similar to Figure 14 and the Universal time was converted to longitude and latitude using world maps calculated by computers from OSO-B2 orbit parameters. This method is accurate to within about a degree for either longitude or latitude near the satellite orbit ascending or descending nodes. It is at these nodes that the satellite is changing geographic coordinates more rapidly than at any other point in the orbit. The isointensity contours were obtained by visual curve fitting to scattered data points and as a result a given contour is no more than ± 5 degrees latitude or longitude in accuracy.

The proton omnidirectional flux was obtained by noting that the Pb-glass isointensity contours overlap that of the scintillator a 30 degrees W longitude and 0 degrees latitude. At this point the scintillator count rate should be the sum of the proton and electron components.

G_p is equal to 20.4 for an energy spectrum exponent of n = 2. N = 2 is the experimentally determined exponent for 600 km altitudes (Armstrong et al., 1961; Naugle and Kniffen, 1963).

The uncertainty introduced in J(>E) by the conversion factors G_p and G_e are equal to 32% and 5.2% respectively if it is assumed that α_{min} is accurate to within $\pm 10°$ and the threshold uncertainty is 20%.

The observed omnidirectional proton fluxes are within 15 to 20% of those found by Paulikas and Freden (1964). The general isointensity contours obtained here seem to be shifted westward and toward the north about 10 degrees in comparison with those of Paulikas and Freden.

Omnidirectional electron fluxes for energies greater than 20 Kev are found to be on the order of 10^{+3} electrons/ cm^2-sec. This value is a factor of 100 less than the fluxes observed at 1000 km but one should expect a possible 10^{-2} decrease over a 400 km altitude change due to increased atmospheric density.

The much shorter "tail" toward the east for electron isointensity contours as opposed to proton contours may be a possible indication of relatively large electron losses into the earth's atmosphere in SARA. As the electrons, trapped in the earth's atmosphere spiral around field lines

they oscillate in a north-south direction being mirrored in the north and south magnetic pole regions. Superimposed on this motion is a drift of the electron guiding centers from west to east. This drift will carry electrons into the Anomaly at its westerly edge. Characteristic values for the drift period around the earth (T_R), the north-south oscillation period (T_B), and the spiral period around a field lines (T_c) are given in Table 4 for three electron kinetic energies. The earth's magnetic field intensity at 1.25 earth radii over the magnetic equator was estimated to be .136 gauss assuming a magnetic moment of 8.1×10^{25} gauss-cm^3 for the earth.

As the electrons drift across the anomaly while oscillating in a north-south direction on a guiding center, depletion of the electron flux will result due to increased atmospheric absorption as the mirroring points decrease and then increase in altitude during the drift across the anomaly. This effect is observed in a plot (Figure 17) for 600 Kev electrons of the percentage decrease in electron flux from the 5.59×10^3 to $.65 \times 10^3$ electrons/cm^2-sec contours as a function of the number of electron oscillations as the guiding center drifts along the L = 1.25 magnetic "shell". The L "shell" is one of the McIlwain (1961) B and L parameters

Table 4

E (Mev)	.06	.6	1
a (cm)	5.2×10^{3}	2.1×10^{4}	2.2×10^{4}
T_c (sec)	$.26 \times 10^{-6}$	2.6×10^{-6}	4.3×10^{-6}
T_b (sec)	3.0×10^{-3}	7.2×10^{-3}	11.0×10^{-3}
T_R (sec)	4.1×10^{3}	2.5×10^{3}	3.8×10^{3}

a: gyration radius

T_c: gyration period

T_b: north-south oscillation period

T_R: drift period around the earth

E : electron kinetic energy

which describes the drift path of a particular guiding center having magnetic equatorial radius of 1.25 earth radii.

Inspection of Figure 17 reveals that the percentage absorption per oscillation is higher for the high isointensity contour values. This is to be expected since the atmospheric altitude at which the mirroring point occurs is less by a factor of 100. The relative increase in altitude for the mirror points as a function of number of oscillations into the anomaly is also plotted in Figure 17.

Conclusions

1. The geographic proton flux distributions indicated by the response of the scintillation detector agree with the results of other measurements with a possible northward shift indicated. No absolute flux determinations are possible because of the uncertain geometric factor for the counter.

2. The South Atlantic Radiation Anomaly appears to act as an electron dump into the earth's atmosphere at satellite altitudes of about 600 km. The data permits an estimate of the loss factor vs assumed effective energy defined by the Cerenkov detectors, but an energy spectrum determination would be required to obtain quantitative results.

3. The isointensity contours presented here are necessarily subject to uncertainties introduced by visual curve-smoothing, limited sampling, varying look angles, and possible time variations in the anomalous region. These factors could introduce uncertainties in the location of contour lines at least as great as $\pm$ five geographic degrees.

Figure 1

Contours of the Total Geomagnetic Field

Intensity in Gauss at the Earth's Surface

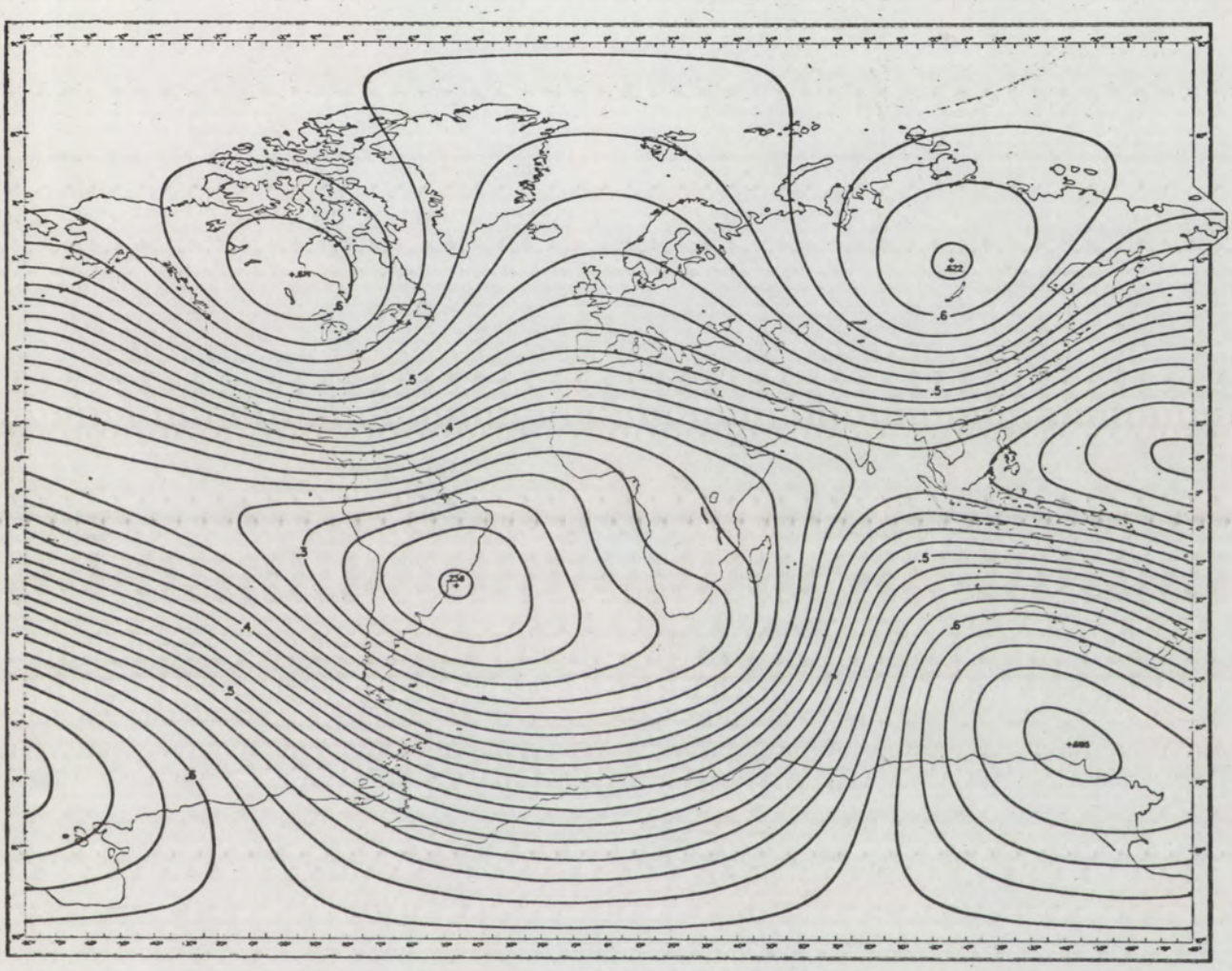

Contours of the Total Geomagnetic Field Intensity in Gauss at the Earth's Surface. All Centers are "Highs" except the South Atlantic Low of .238 Gauss. (Cain, 1965)

Figure 2

Plot of Proton Flux Isointensity Contours. Lines of constant L at these altitudes are also shown. The smaller numbers represent typical altitudes where the data were taken. (Paulikas and Freden, 1964)

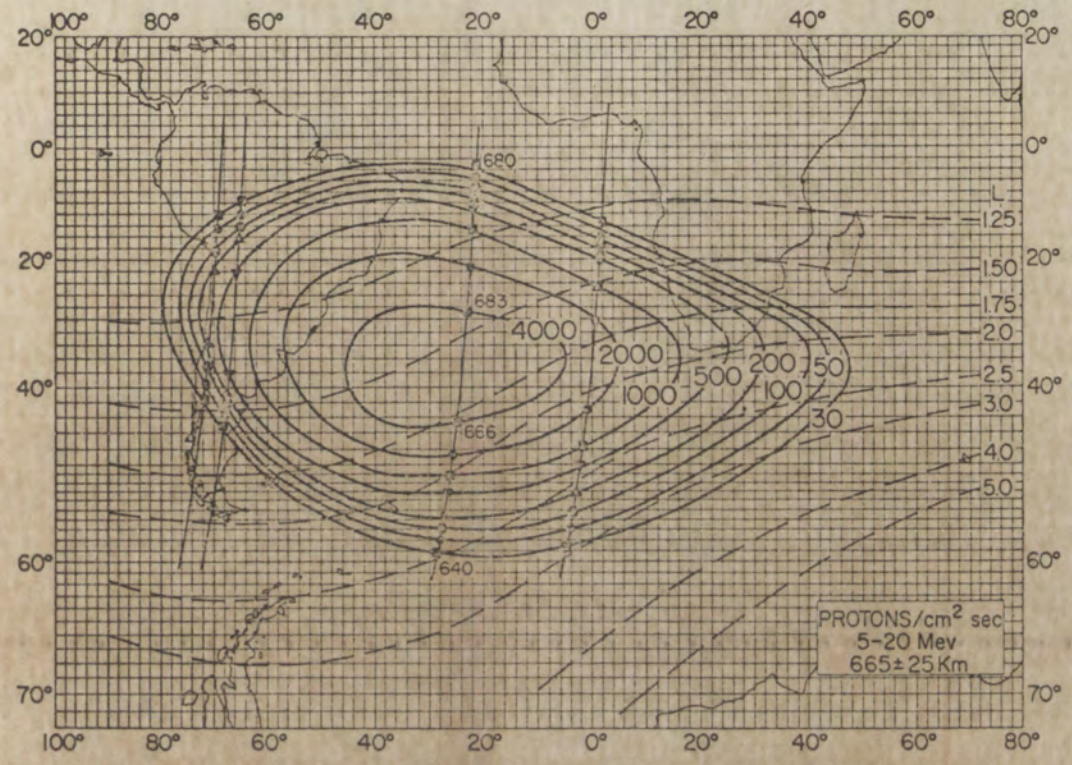
100° 80° 60° 40° 20° 0° 20° 40° 60° 80°
20° 0° 20° 40° 60° 70°
680
683
666
640
4000
2000
1000
500
200
100
50
30
L
1.25
1.50
1.75
2.0
2.5
3.0
4.0
5.0
PROTONS/cm² sec
5-20 Mev
665± 25 Km

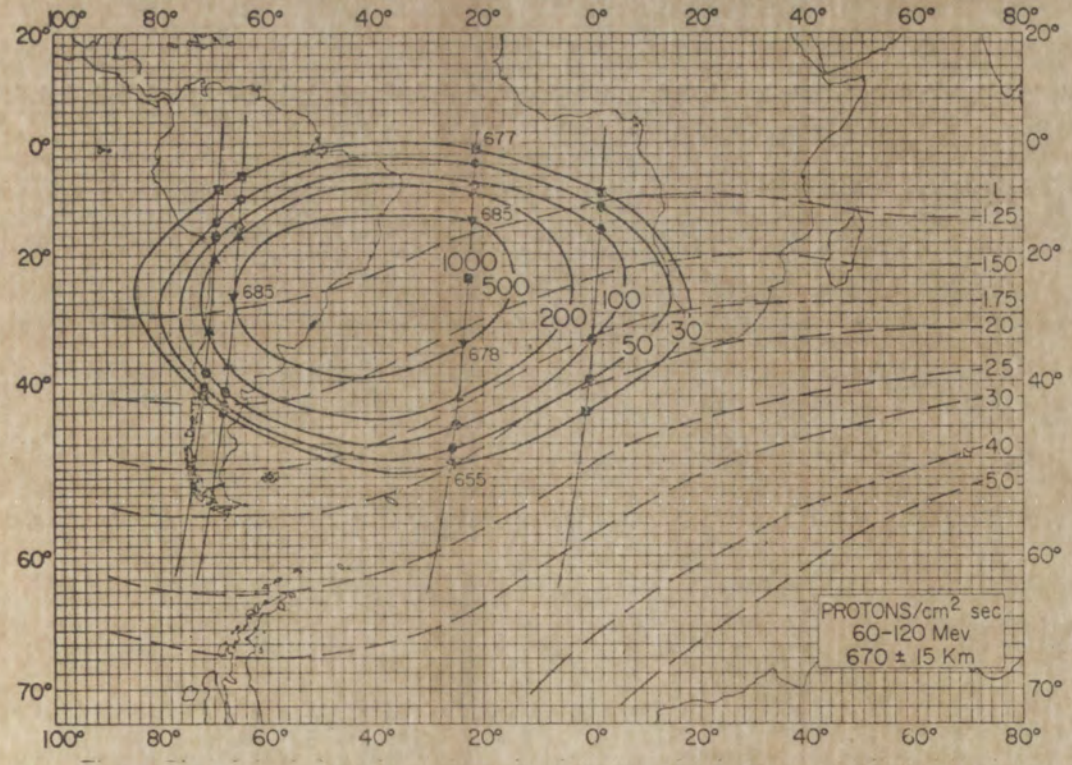
100° 80° 60° 40° 20° 0° 20° 40° 60° 80°
20° 0° 20° 40° 60° 70°
677
685
685
678
655
1000
500
200
100
50
30
L
1.25
1.50
1.75
2.0
2.5
3.0
4.0
5.0
PROTONS/cm² sec
60-120 Mev
670 ± 15 Km

Figure 3

Geographic Location of the Mirroring Protons

The mean coordinate of the region (30 deg. S, 41 deg. W) is shown as an open circle with accompanying error bars. Isogonic lines are solid, isoclinic lines are dashed. (Heckman and Nakano, 1963)

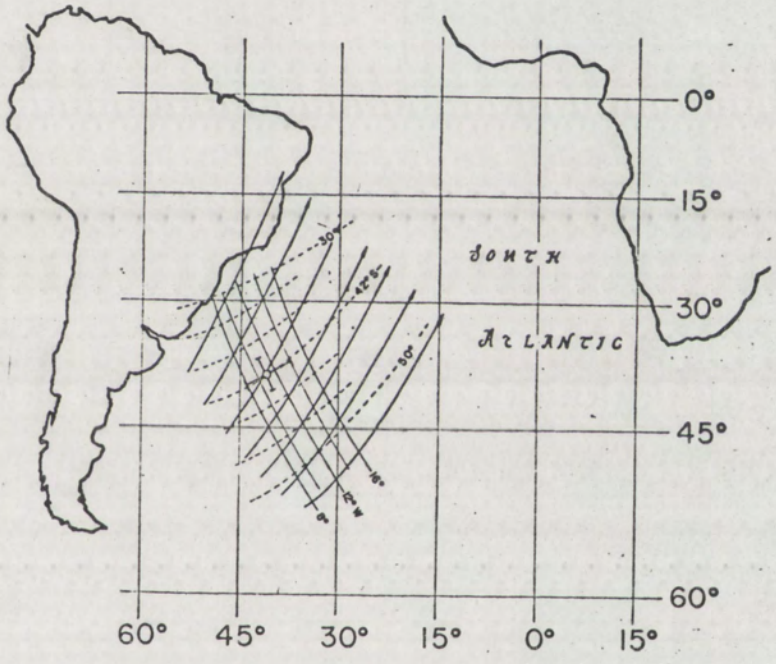
0°
15°
30°
45°
60°
60°
45°
30°
15°
0°
15°
SOUTH
ATLANTIC

Figure 4

OSO-B2 Orbiting Solar Observatory

OSO-B2 ORBITING SOLAR OBSERVATORY

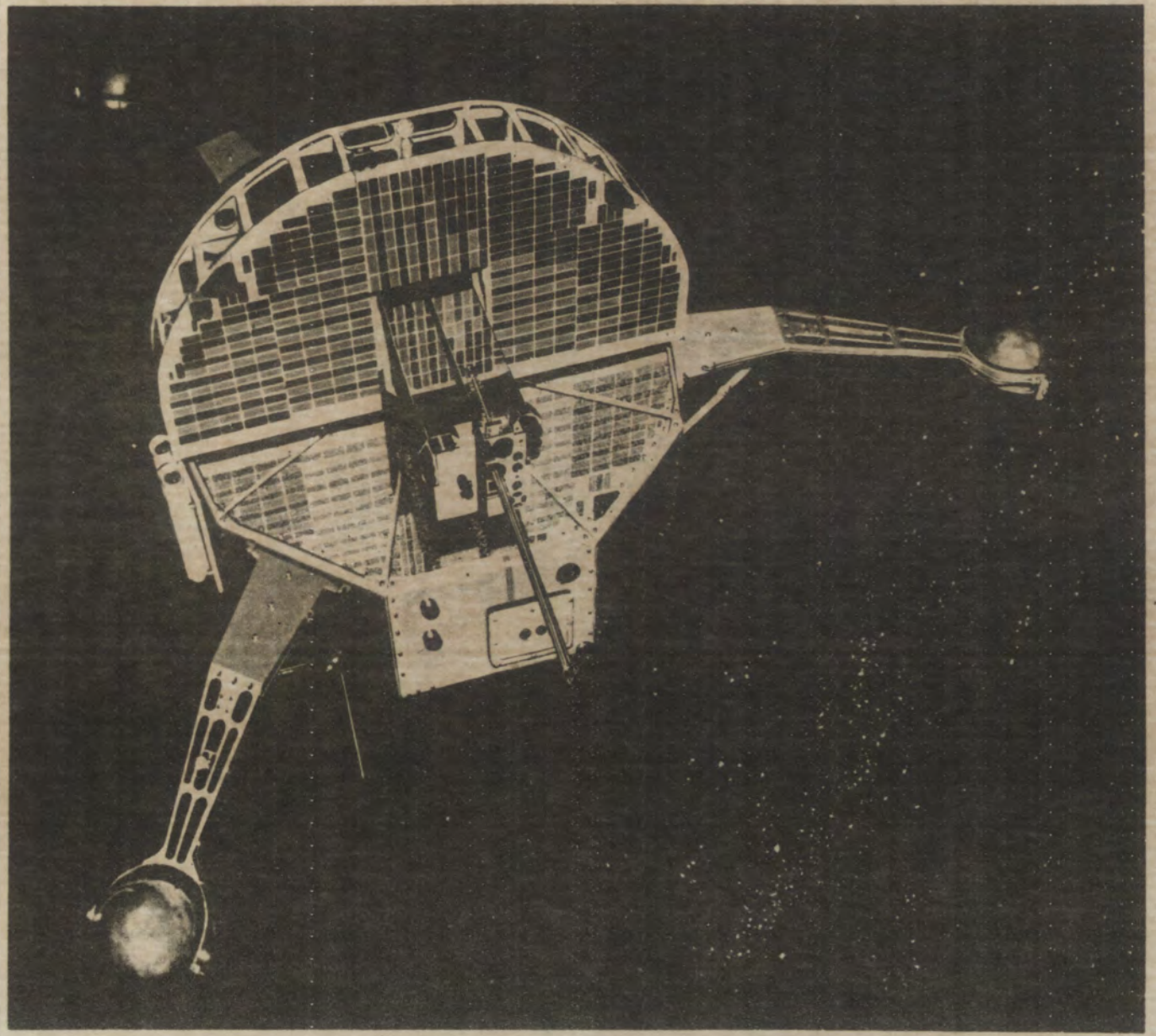

PROGRAM SUMMARY

PROJECT: *OSO-B2 ORBITING SOLAR OBSERVATORY*

PROJECT DIRECTION:
NASA/GODDARD SPACE FLIGHT CENTER

PRIME CONTRACTOR:
BALL BROS. RESEARCH CORP.

EXPERIMENTERS:
GODDARD SPACE FLIGHT CENTER
AMES RESEARCH CENTER
HARVARD OBSERVATORY
UNIVERSITY OF NEW MEXICO
UNIVERSITY OF MINNESOTA
NAVAL RESEARCH LABORATORIES

MAJOR OBJECTIVES:
MEASURE ELECTROMAGNETIC RADIATION IN THE ULTRAVIOLET, X-RAY & GAMMA RAY REGIONS OF THE SPECTRUM & TO STUDY TIME VARIATIONS OF THESE EMISSIONS

LIFETIME:
ESTIMATED: SIX MONTHS

LAUNCH VEHICLE:
DELTA

CIRCULAR ORBIT:
300 NAUTICAL MILES

INCLINATION:
33°

PERIOD:
95 MINUTES

PAYLOAD WEIGHT:
549.7 lbs. (Experimental Wt. 215 lbs.)

POINTING ACCURACY:
1 MINUTE OF ARC

SCAN RASTER:
40×40 MINUTES OF ARC

Figure 5

OSO-B2 Satellite Wheel Experiments

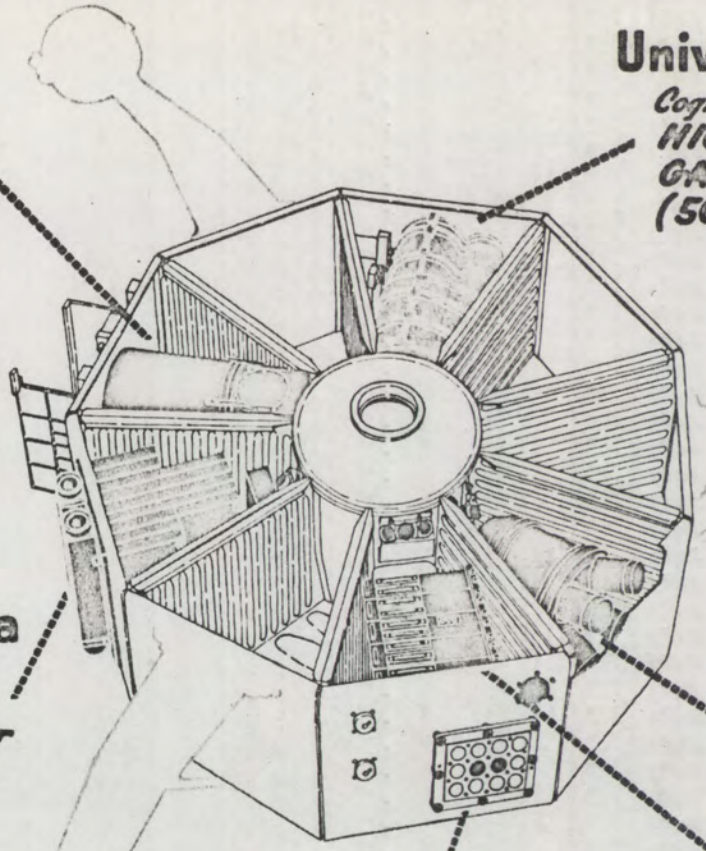

Goddard Space Flight Center
SOLAR PHYSICS
Cognizant Scientist: Dr. K. Hallam
ULTRAVIOLET SPECTRO-PHOTOMETER (1500 Å to 3300 Å)

Univ. of New Mexico
Cognizant Scientist: Dr. C.P. Leavitt
HIGH ENERGY GAMMA RAY TELESCOPE (50 Mev to 1 Bev)

Univ. of Minnesota
Cognizant Scientist: Dr. E. Ney
ZODIACAL LIGHT TELESCOPES (WHITE LIGHT-ORTHOGONAL POLARIZATIONS)

Goddard Space Flight Center
SOLAR PHYSICS
Cognizant Scientist: Mr. K. Frost
LOW ENERGY GAMMA RAY TELESCOPE (0.1 Mev to 3 Mev)
ELECTRONICS FOR THE ULTRAVIOLET SPECTRO-PHOTOMETER & THE LOW ENERGY GAMMA RAY TELESCOPE

Ames Research Center
Cognizant Scientist: Mr. C. Neel
EMISSIVITY DETECTORS

WHEEL EXPERIMENTS

Figure 6

Typical OSO-B2 Satellite Orbit

Plotted in Geographic Coordinates

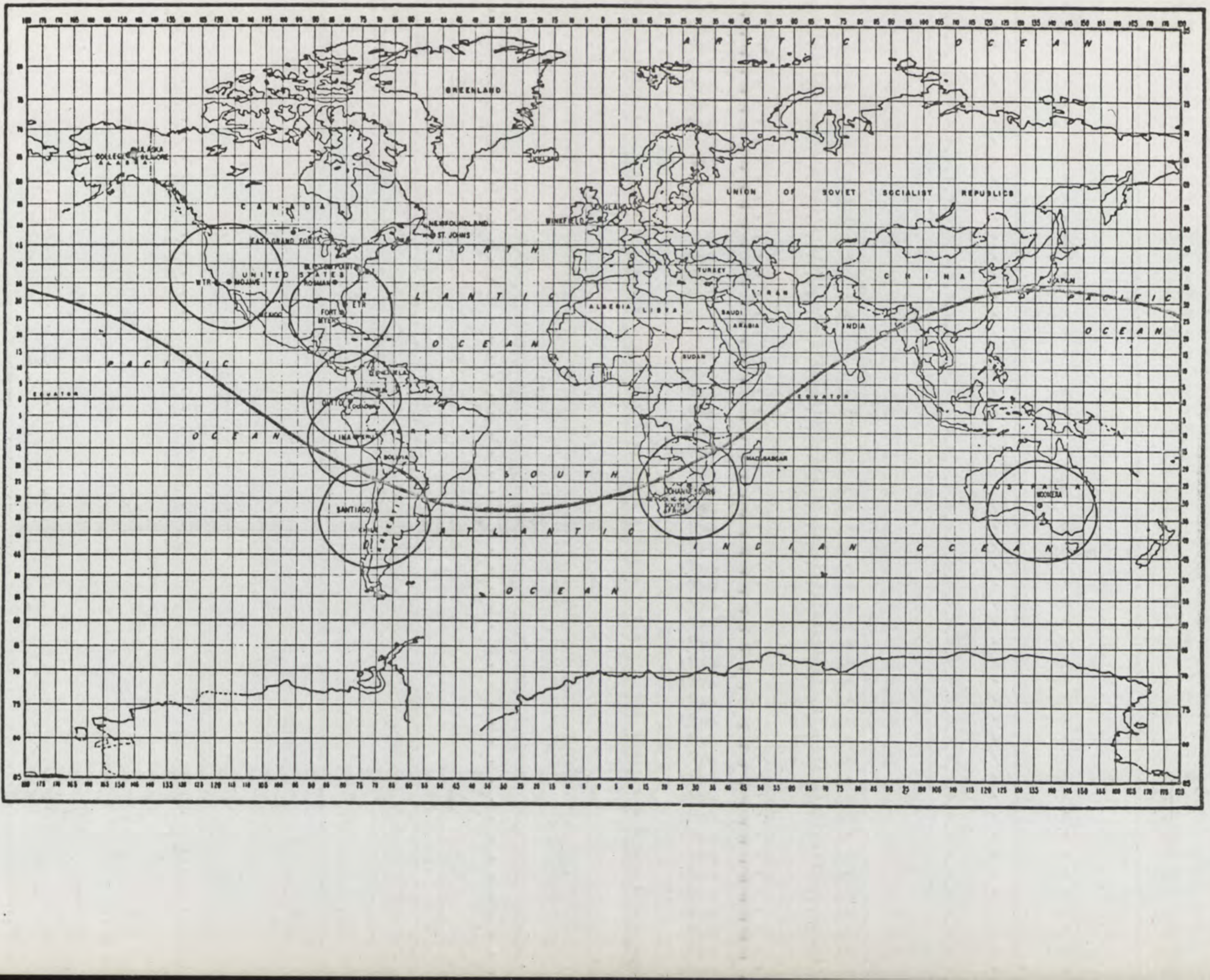

ARCTIC OCEAN
GREENLAND
ALASKA
CANADA
UNITED STATES
MOJAVE
ST. JOHNS
NEWFOUNDLAND
NORTH ATLANTIC OCEAN
PACIFIC OCEAN
EQUATOR
FORT MYERS
MEXICO
SANTIAGO
CHILE
BOLIVIA
SOUTH ATLANTIC OCEAN
UNION OF SOVIET SOCIALIST REPUBLICS
CHINA
JAPAN
INDIA
IRAN
TURKEY
ALGERIA
LIBYA
SAUDI ARABIA
SUDAN
MADAGASCAR
SOUTH AFRICA
INDIAN OCEAN
AUSTRALIA
WOOMERA

Figure 7

OSO-B2 Satellite Space

Orientation Control Systems

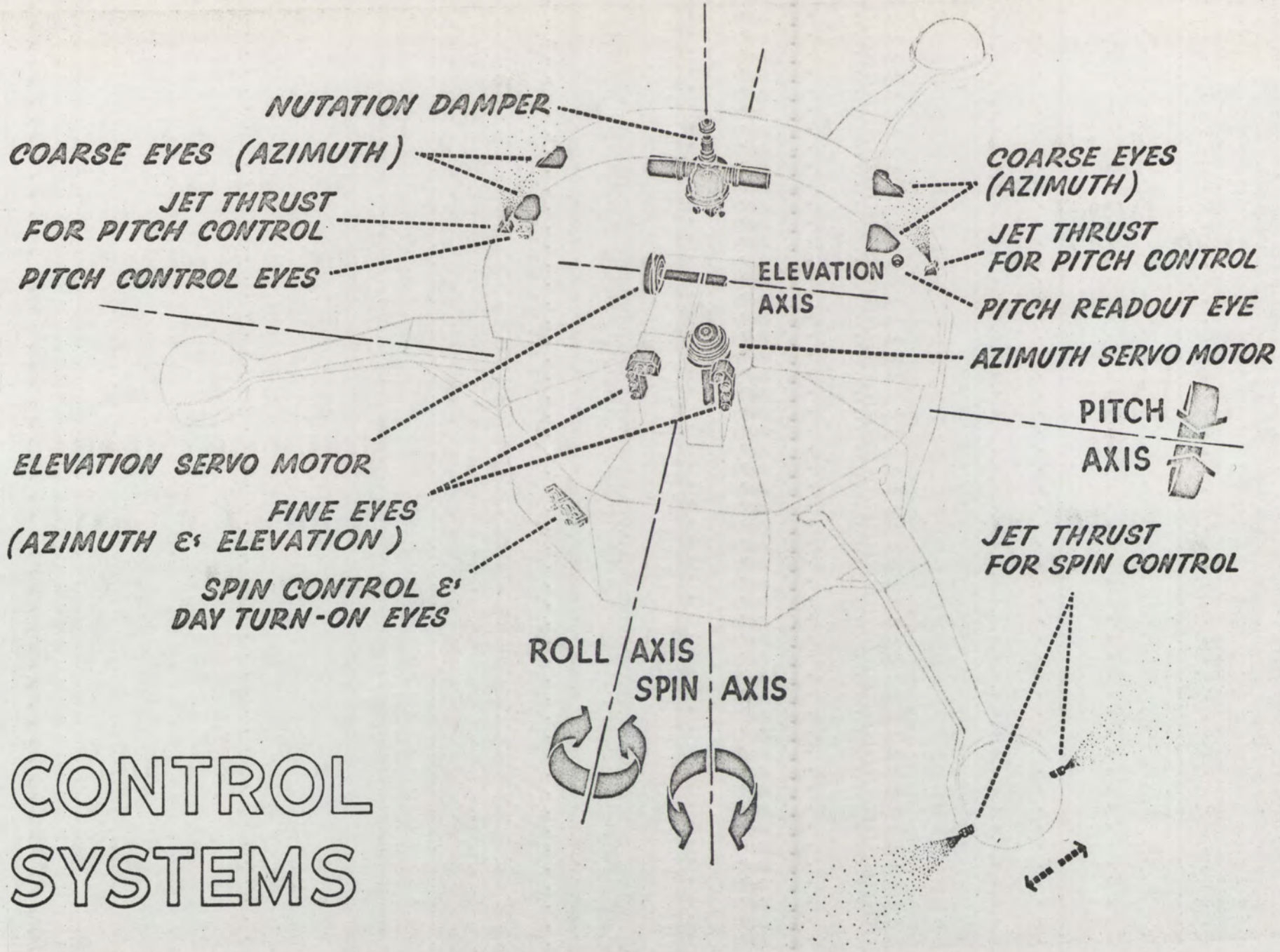

CONTROL SYSTEMS

Figure 8

Gamma Ray Telescope Flown

in OSO-B2 Satellite

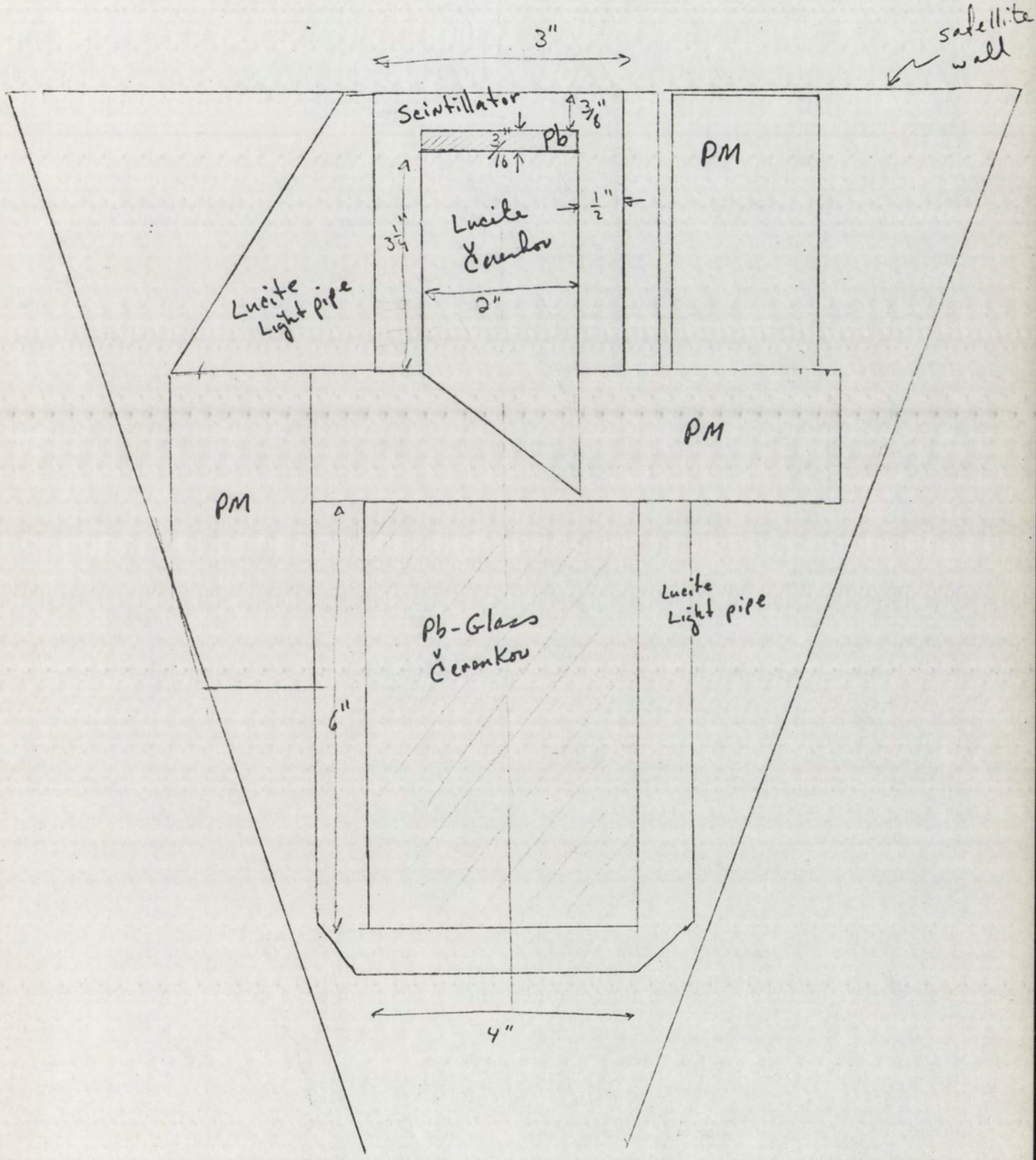
3"
satellite wall
Scintillator
3/16"
Pb
3/16
PM
3 1/4"
Lucite Čerenkov
1/2"
Lucite Light pipe
2"
PM
PM
Pb-Glass Čerenkov
Lucite Light pipe
6"
4"

Figure 9

Relative Changes in Satellite Wheel

Skin Temperatures Over One Orbit

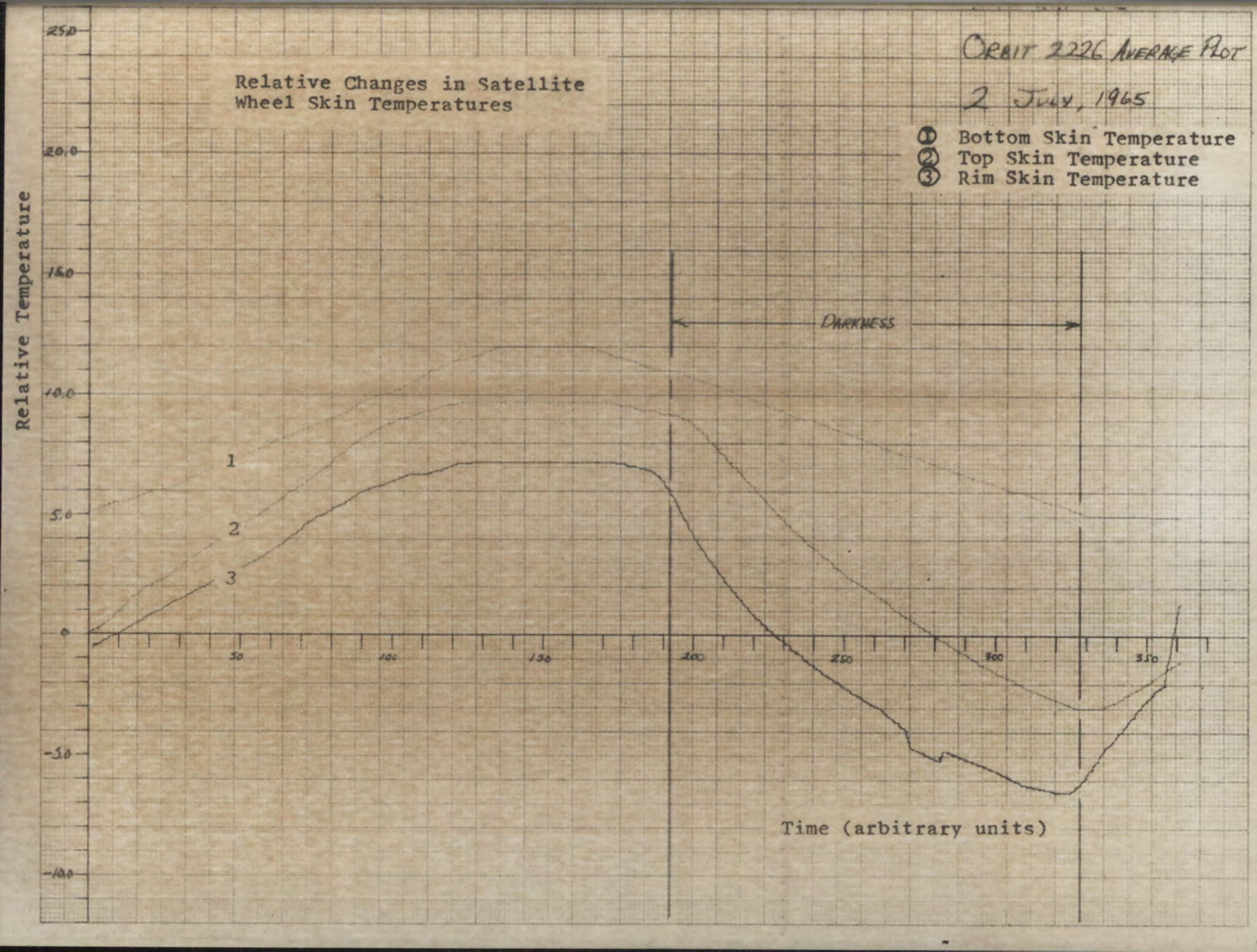
Relative Changes in Satellite Wheel Skin Temperatures
Orbit 2226 Average Plot
2 July, 1965
① Bottom Skin Temperature
② Top Skin Temperature
③ Rim Skin Temperature
Relative Temperature
25.0
20.0
15.0
10.0
5.0
0
-5.0
-10.0
Darkness
1
2
3
50
100
150
200
250
300
350
Time (arbitrary units)

Figure 10

Scintillation Counter Calibration Curve

Volts vs Counts/sec

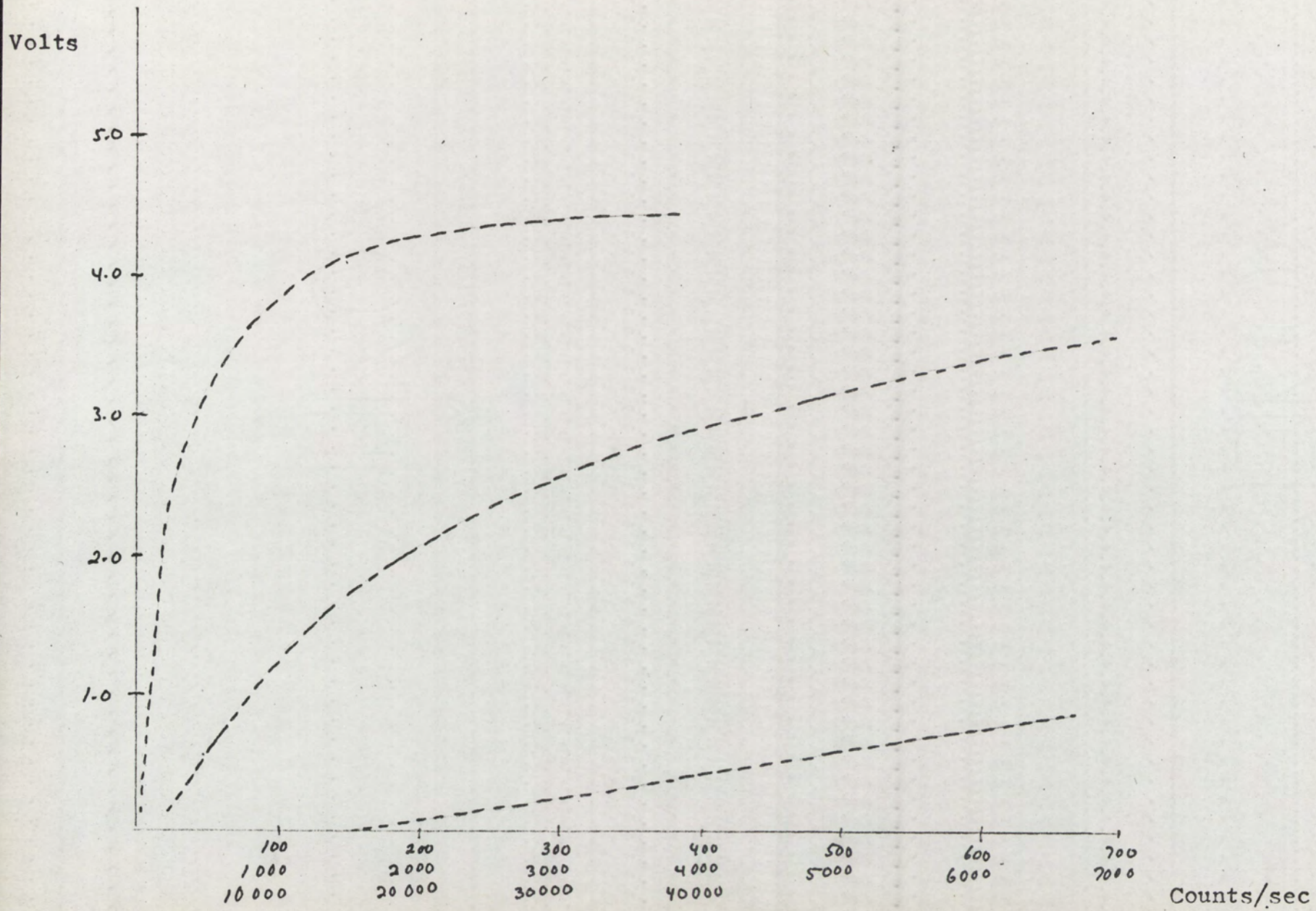
Volts
5.0
4.0
3.0
2.0
1.0
100
1 000
10 000
200
2 000
20 000
300
3000
30000
400
4 000
40000
500
5000
600
6000
700
7000
Counts/sec

Figure 11

Lucite Cerenkov Counter Calibration Curve

Volts vs Counts/sec

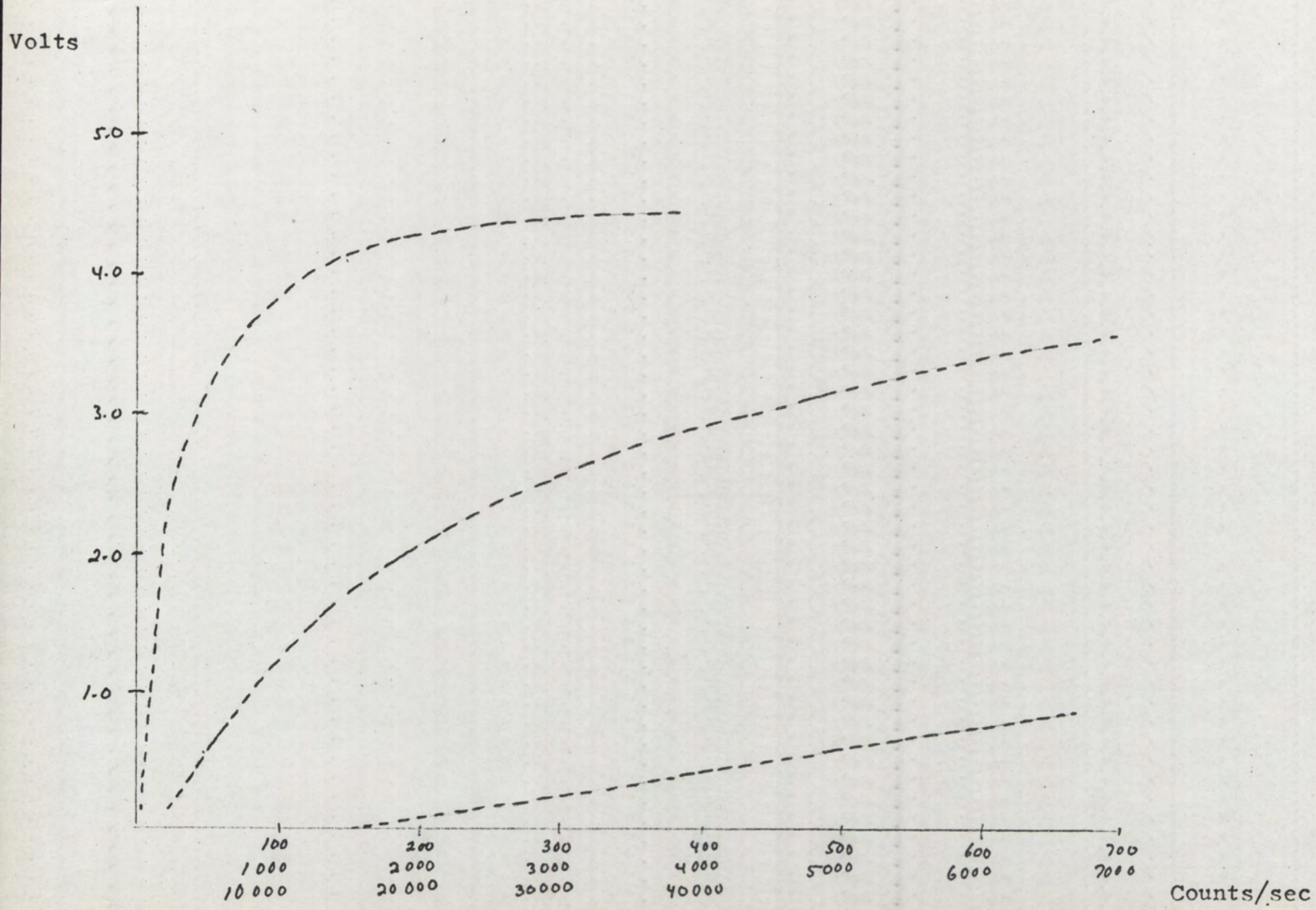
Volts
5.0
4.0
3.0
2.0
1.0
100
1 000
10 000
200
2 000
20 000
300
3000
30000
400
4 000
40000
500
5000
600
6000
700
7000
Counts/sec

Figure 12

Pb-Glass Cerenkov Counter Calibration Curve

Volts vs Counts/sec

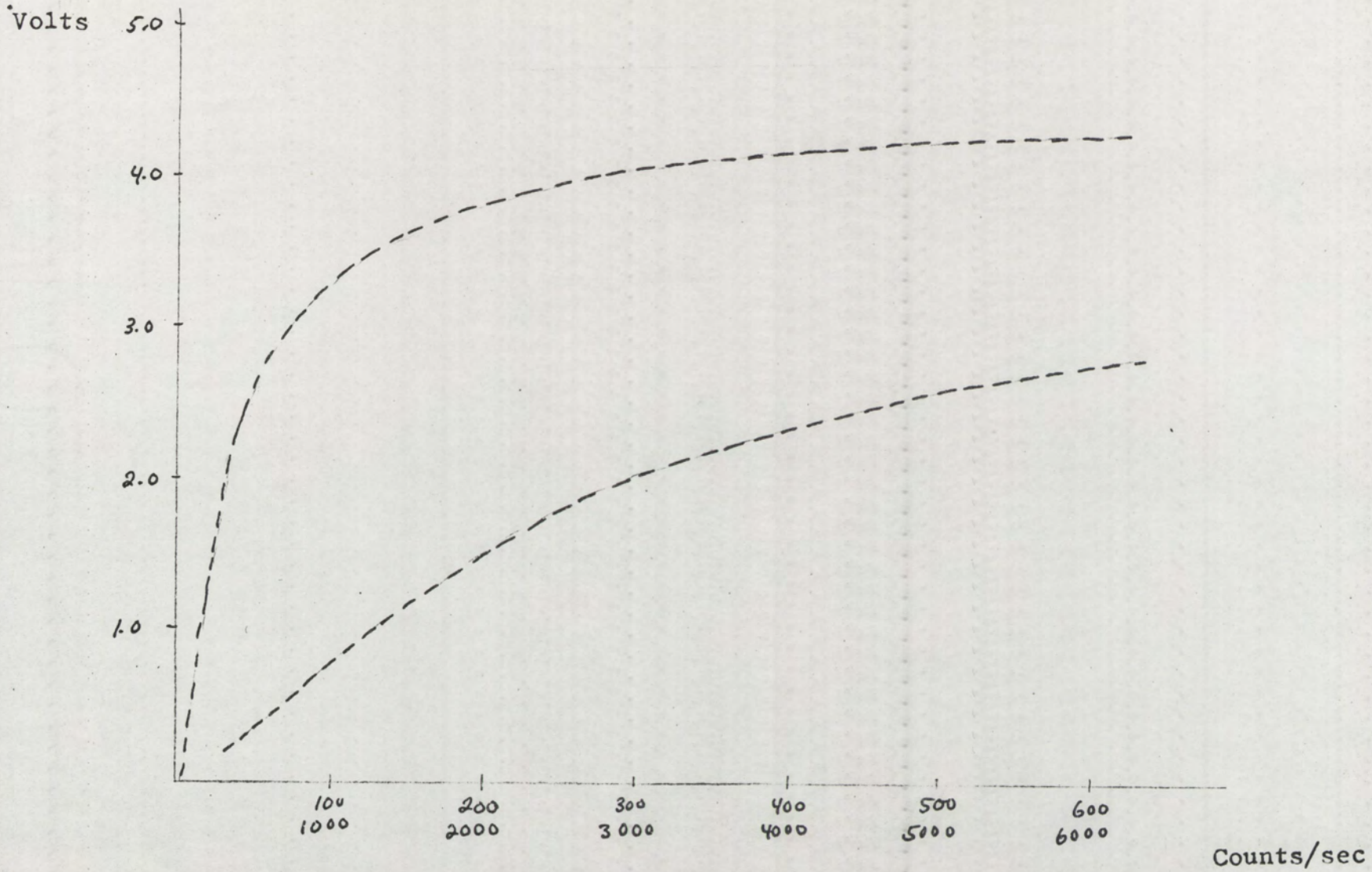
Volts
5.0
4.0
3.0
2.0
1.0
100
1000
200
2000
300
3000
400
4000
500
5000
600
6000
Counts/sec

Figure 13

The Threshold Kinetic Energies for Cerenkov Radiation from the Elementary Particles, as a function of the Refractive Index of the medium

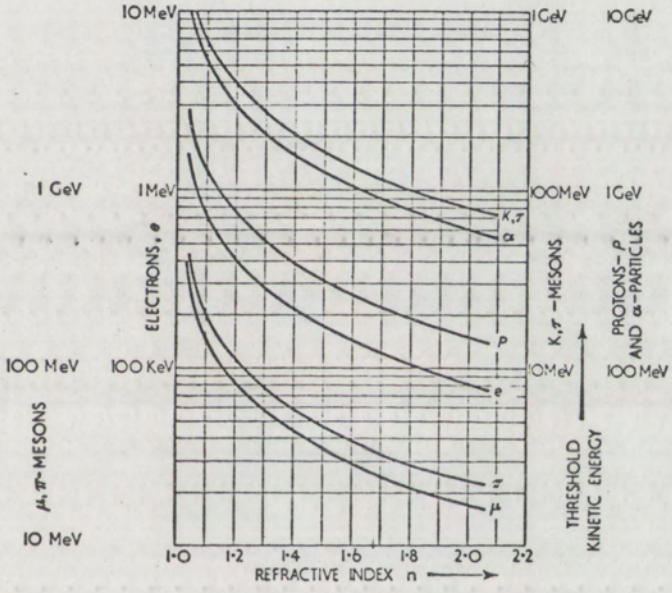
10 MeV
1 GeV
10 GeV
1 GeV
1 MeV
100 MeV
1 GeV
100 MeV
100 KeV
10 MeV
100 MeV
10 MeV
ELECTRONS, e
μ, π - MESONS
K, π - MESONS
PROTONS - p AND α - PARTICLES
THRESHOLD KINETIC ENERGY
K, π
α
p
e
π
μ
1·0
1·2
1·4
1·6
1·8
2·0
2·2
REFRACTIVE INDEX n

Figure 14

Typical Satellite Readout Data Over One Orbit for the Scintillation, Pb-Glass Cerenkov, and Lucite Cerenkov Counters

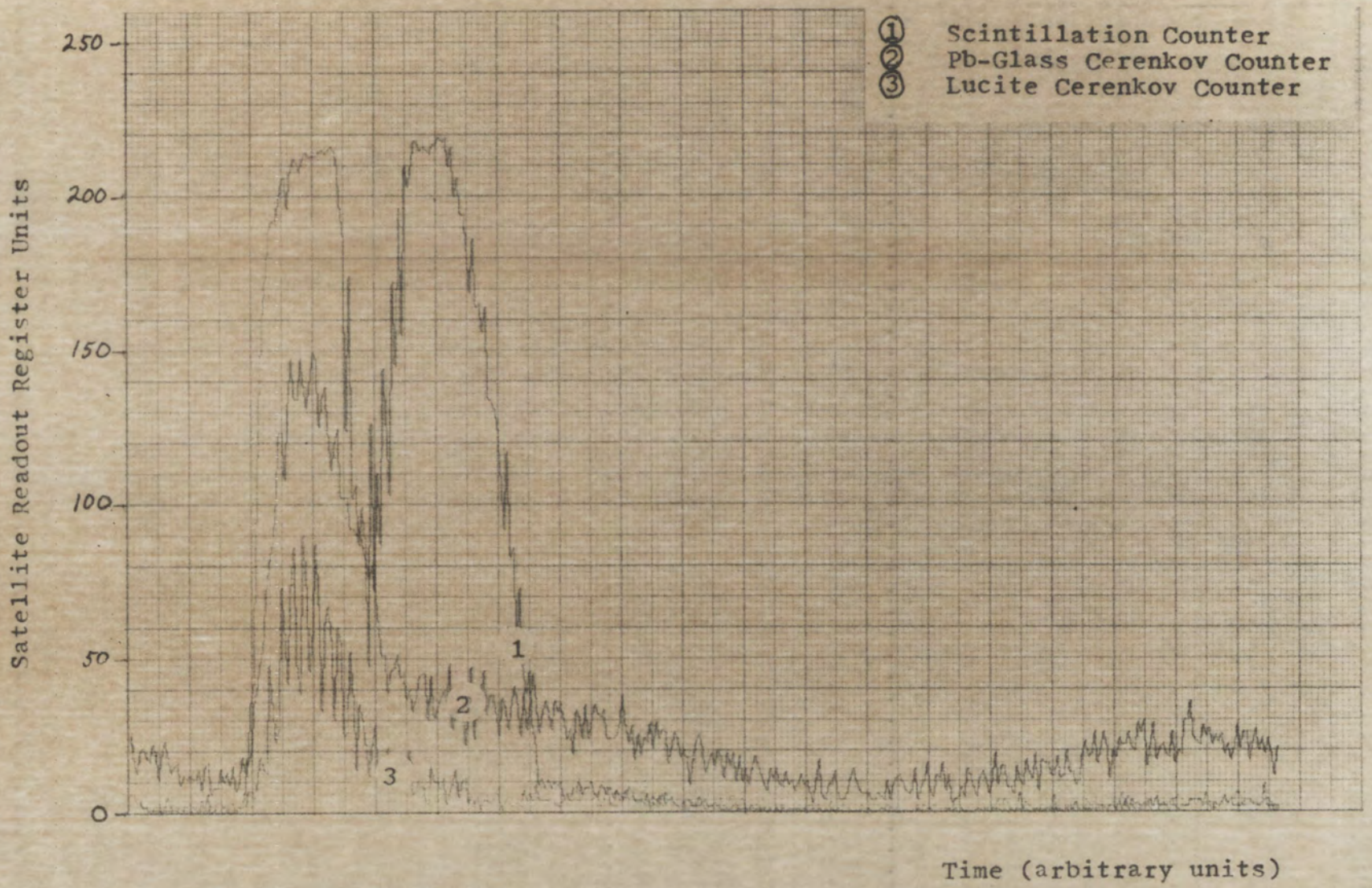
① Scintillation Counter
② Pb-Glass Cerenkov Counter
③ Lucite Cerenkov Counter
250
200
150
100
50
0
Satellite Readout Register Units
1
2
3
Time (arbitrary units)

Figure 15

Isointensity Contours for Proton Fluxes

for Energies Greater Than 2 Mev

Altitude: 592 $\pm$ 40 kilometers

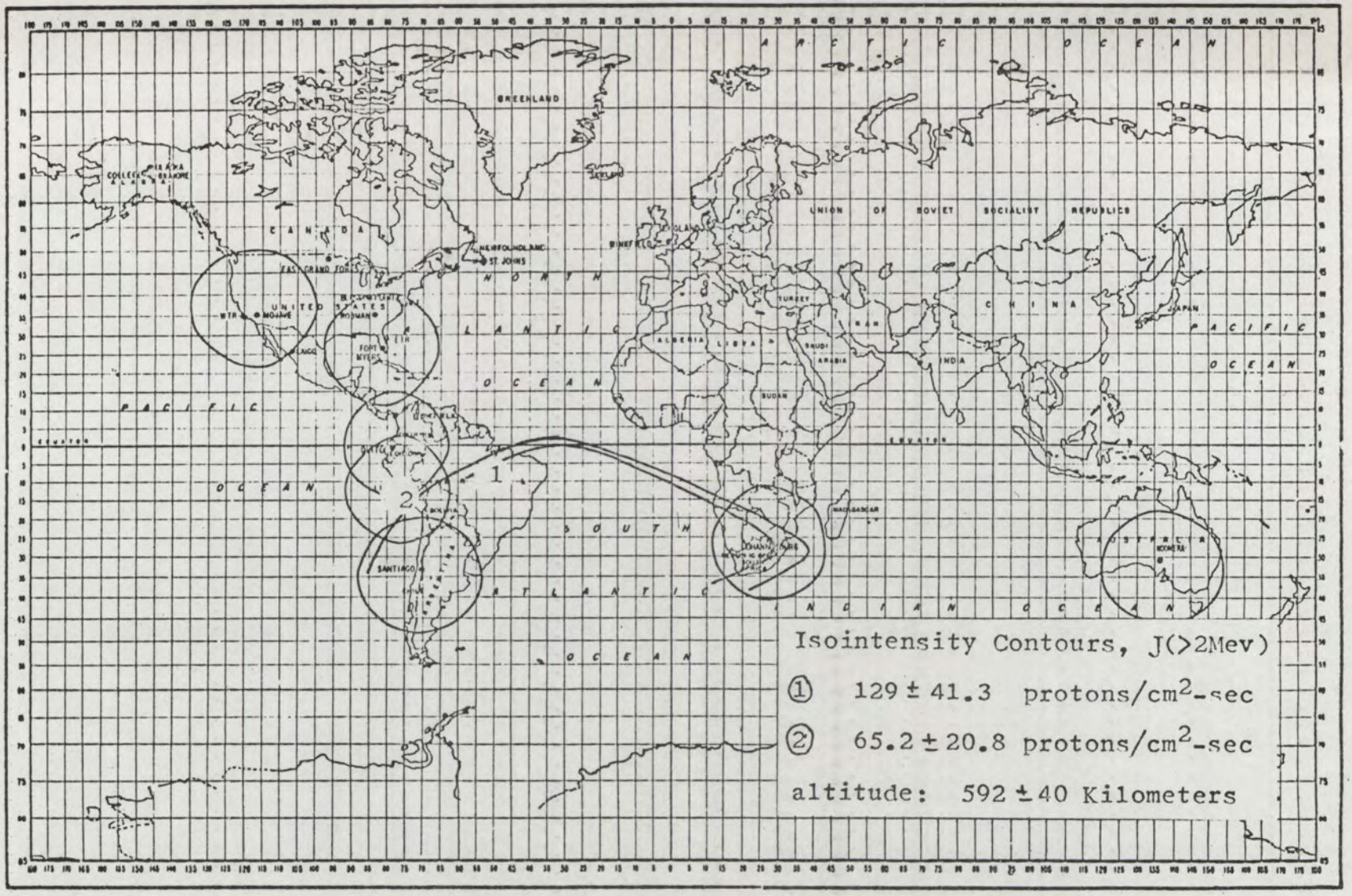
GREENLAND
CANADA
UNITED STATES
UNION OF SOVIET SOCIALIST REPUBLICS
CHINA
INDIA
JAPAN
AUSTRALIA
NORTH ATLANTIC OCEAN
PACIFIC OCEAN
SOUTH ATLANTIC OCEAN
INDIAN OCEAN
ARCTIC OCEAN
EQUATOR
SANTIAGO
1
2
Isointensity Contours, J(>2Mev)
① 129 ± 41.3 protons/cm²-sec
② 65.2 ± 20.8 protons/cm²-sec
altitude: 592 ± 40 Kilometers

Figure 16

Constant Magnetic Field Intensity, B (gauss)

Constant Magnetic Shell Parameter, L (earth radii)

Altitude: 592 $\pm$ 40 kilometers

Isointensity contours for electron fluxes for energies greater than 20 Kev

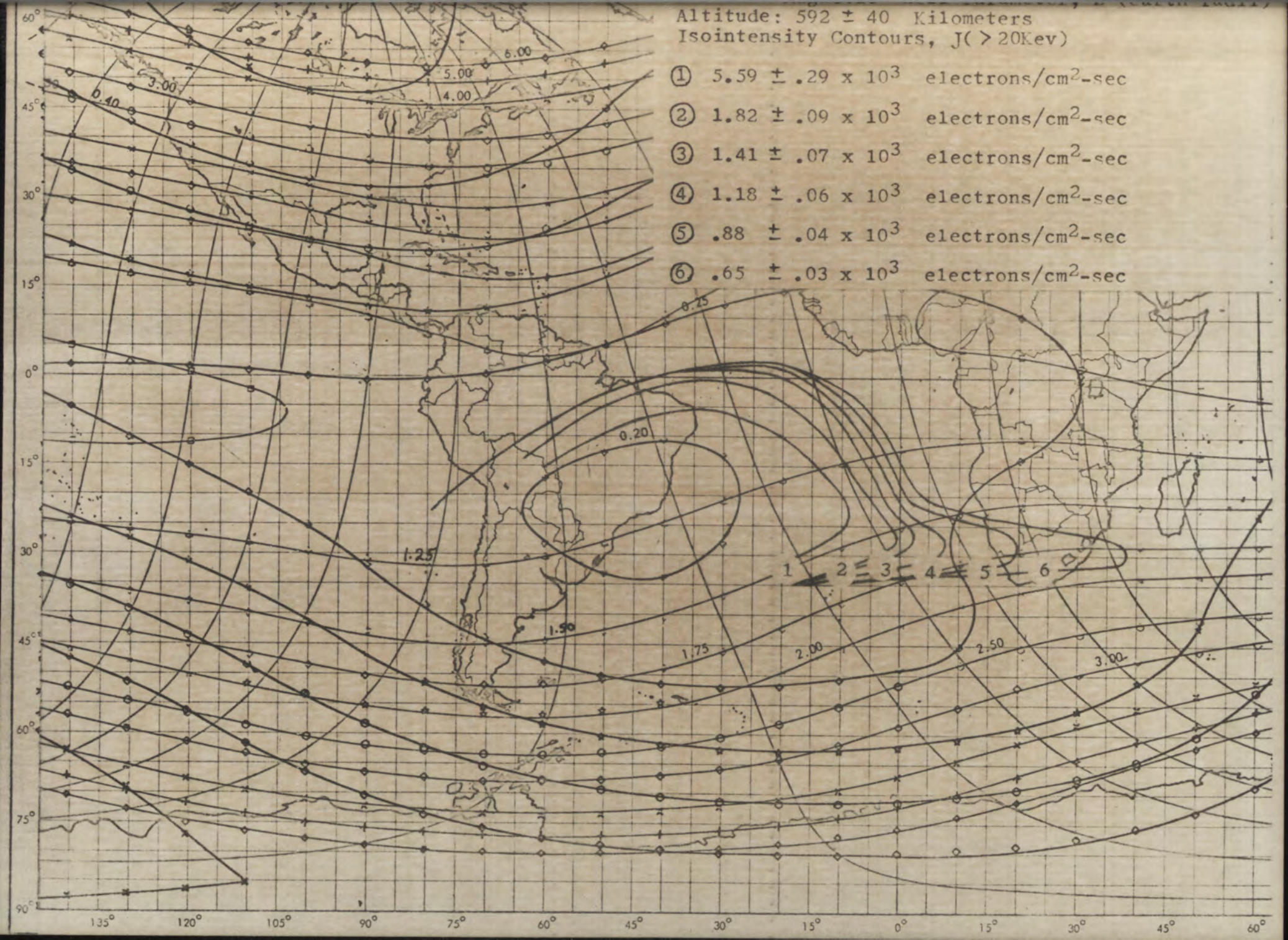
Altitude: 592 ± 40 Kilometers
Isointensity Contours, J(> 20Kev)
① 5.59 ± .29 x 10³ electrons/cm²-sec
② 1.82 ± .09 x 10³ electrons/cm²-sec
③ 1.41 ± .07 x 10³ electrons/cm²-sec
④ 1.18 ± .06 x 10³ electrons/cm²-sec
⑤ .88 ± .04 x 10³ electrons/cm²-sec
⑥ .65 ± .03 x 10³ electrons/cm²-sec
6.00
5.00
4.00
3.00
0.40
0.25
0.20
1.25
1.50
1.75
2.00
2.50
3.00
1
2
3
4
5
6
60°
45°
30°
15°
0°
15°
30°
45°
60°
75°
90°
135°
120°
105°
90°
75°
60°
45°
30°
15°
0°
15°
30°
45°
60°

Figure 17

Percentage Electron Flux Loss vs Number of Oscillations into the South Atlantic Radiation Anomaly. Relative altitude change in the anomaly vs number of oscillations

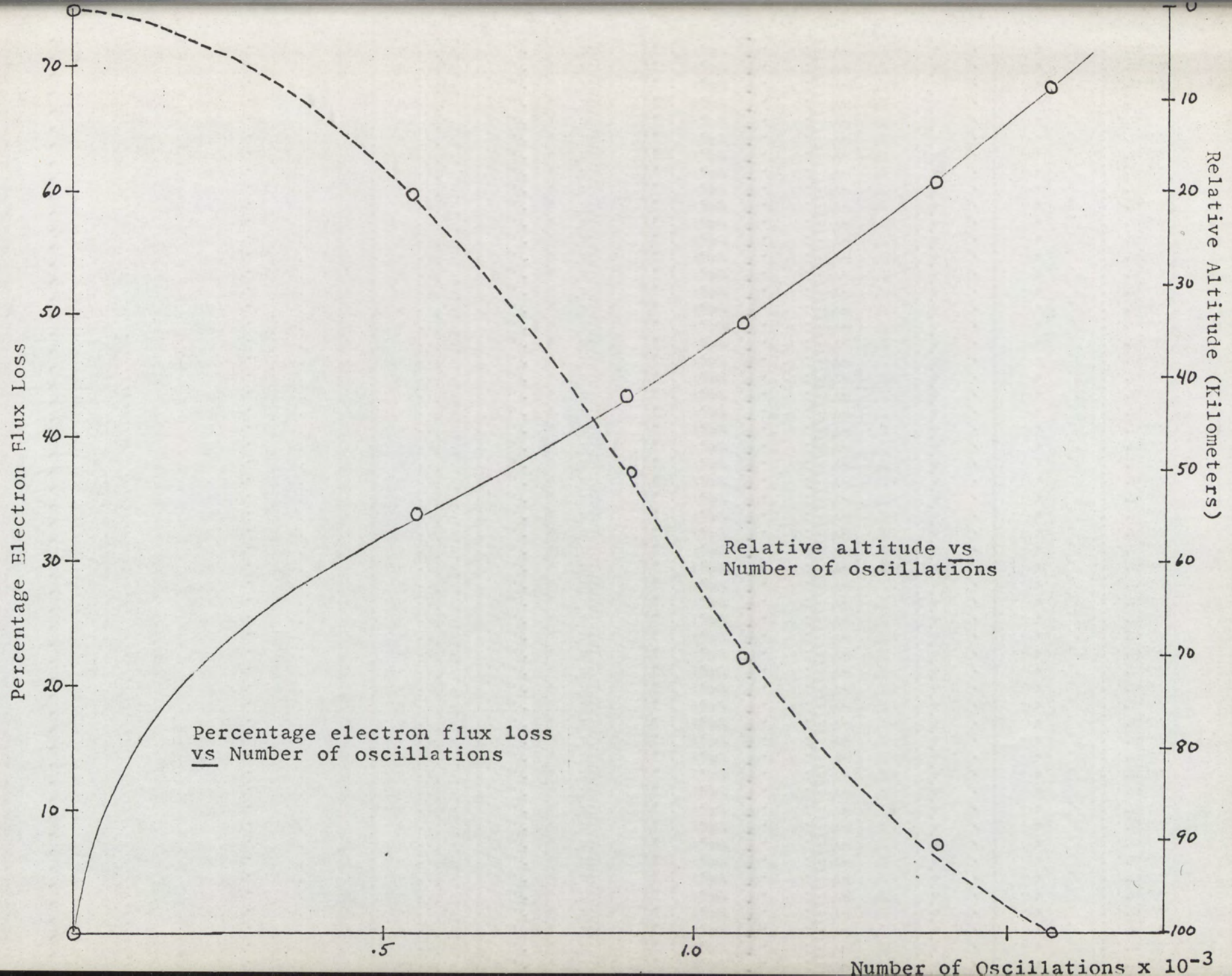
Percentage Electron Flux Loss
70
60
50
40
30
20
10
Relative Altitude (Kilometers)
10
20
30
40
50
60
70
80
90
100
Relative altitude vs
Number of oscillations
Percentage electron flux loss
vs Number of oscillations
.5
1.0
Number of Oscillations x 10^{-3}

References

Armstrong, A. H., F. B. Harrison, H. H. Heckman, and L. Rosen; J. Geophys. Res., 65, 1377-1383, (1960)

Bloom, Mann, and West; The Electron Spectrum from 90 to 1200 Kev as Observed on Discoverer Satellites 29 and 31, paper delivered at COSPAR Meeting, Washington, D.C. (April, 1962)

Cain, J. C., et al; J. Geophys. Res., 70, 3647, (1965)

Dessler, A. J.; J. Geophys. Res., 64, 713, (1959)

Dudziak, W., D. D. Kleinecke, and T. J. Kostige; Geographic Displays of Geomagnetic Geometry, Contract DA49-146-XZ-109, Number RM 63TMP-2, G. E. Company, Santa Barbara, California, (April, 1963)

Evans, R. D.; The Atomic Nucleus, McGraw-Hill Co., Inc., (1955)

Freden, S. C. and G. A. Paulikas; J. Geophys. Res., 69, 1259, (1964)

Heckman, H. H. and G. H. Nakano; J. Geophys. Res., 68, 2117, (1963)

Jelley, J. V.; Cerenkov Radiation, Pergamon Press, (1958)

Katz, L. and A. S. Penfold; Revs. Mod. Phys., 24, 28, (1952)

Lenchek, A. M. and S. F. Singer; J. Geophys. Res., 67, 4073, (1962)

NASA-GSFC, Operations Plan 14-64, OSO-B2, December 1964, X-535-64-312

Naugle, J. E. E. and D. A. Kniffin; J. Geophys. Res., 68, 4065, (1963)

Rossi, B.; High Energy Particles, Prentice-Hall, Inc., (1961)

Yoshida, S., et al; J. Geophys. Res., 65, 807, (1960)

Appendix I

Geometric factor for a cylindrical counter

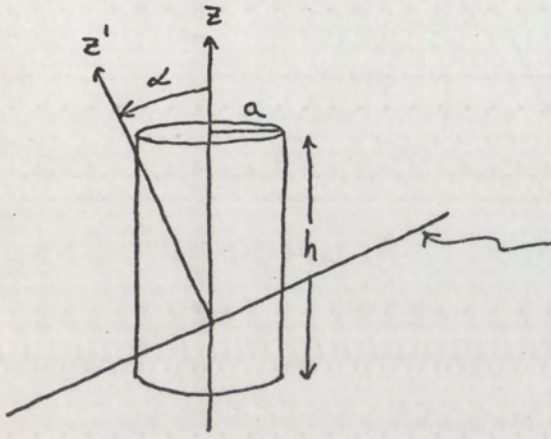

The differential surface area on the cylinder cut by the flux plane is the circumference times dz'. The projection of this circumference onto the x-η plane is an ellipse.

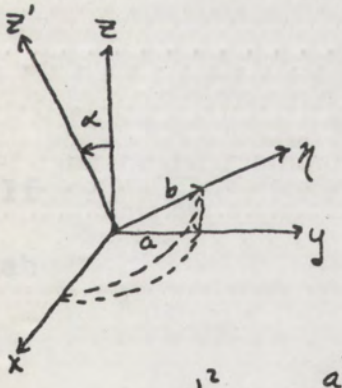

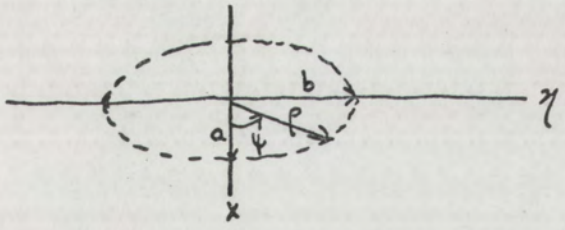

$$b^2 = \frac{a^2}{\cos^2\alpha}$$

$$\rho^2 = \frac{a^2 b^2}{a^2\sin^2\psi + b^2\cos^2\psi}$$

$$k^2 = \sin^2\alpha$$

$$\rho = \frac{a}{\sqrt{1 - k^2\sin^2\psi}}$$

Integration ρ from 0 to $\frac{\pi}{2}$ represents 1/4 the circumference so that the area of the cylinder exposed to a series of

planes of thickness h is

$$A = 4a \int_0^h \int_0^{\pi/2} \frac{dz' d\psi}{\sqrt{1 - k^2 \sin^2 \psi}} = 4ah\,K(\alpha)$$

where $K(\alpha)$ is an elliptic integral of the second kind. The effective areas perpendicular to the flux planes for the cylinder top and sides is

sides: $A_{eff} = 4ah\,K(\alpha)\cos\alpha$

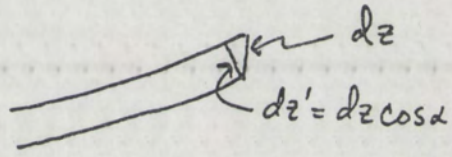

top: $A_{eff} = \pi a^2 \sin\alpha$

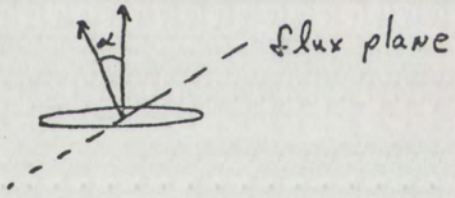

If the flux is assumed to be in the $\theta = 0°$ plane then the absorbing area as a function of φ is equal to

$$A_{abs.} = A_{eff} \sin\varphi$$

and the counting rate at energy E is

$$r(E) = \int_0^{2\pi} \int_0^{\pi/2} I(\theta, \varphi, E)\, A_{abs.} \sin\theta\, d\theta\, d\varphi \quad \text{counts/sec-Mev}$$

which becomes

$$r(E) = \int_0^{\pi} \int_0^{6^\circ} I_0 \sin\theta \, d\theta \, \sin\varphi \, d\varphi \left[4ah \, K(\alpha) \cos\alpha + \pi a^2 \sin\alpha \right]$$

if the flux divergence out of the $\theta = 0^\circ$ plane is $\pm 6^\circ$ and the detector sees no flux for $\varphi > \pi$ where φ is measured from the detector surface.

$$r(E) = I_0 \frac{4a}{2\pi} \left\{ 4h \cos\alpha + \pi a \sin\alpha \right\} \qquad \text{counts/Mev-sec}$$

$$J(E) = \int_0^{2\pi} 2 \int_0^{6^\circ} I_0 \sin\theta \, d\theta \, d\varphi = I_0 \qquad \text{Counts/Mev-cm}^2\text{-sec}$$

The geometric factor times the efficiency for a particular satellite orientation in the anomaly is then

$$r/J(E) = e'g'(E,\alpha) = \frac{2a}{\pi} \left\{ 4h \, K(\alpha) \cos\alpha + \pi a \sin\alpha \right\} \text{ cm}^2$$

The determination of the average $e\,g(E,\alpha)$ per unit time is done by integrating α over 1/4 revolution of the wheel since this corresponds to the angle over which the counters achieve all possible orientations with respect to the anomaly planes. The actual angle over which the counters receive charged particles is less than $\frac{\pi}{2}$ due to the absorption of particles by other wheel compartments in the satellite. The α_{min} are shown in the top view diagram of the wheel compartment.

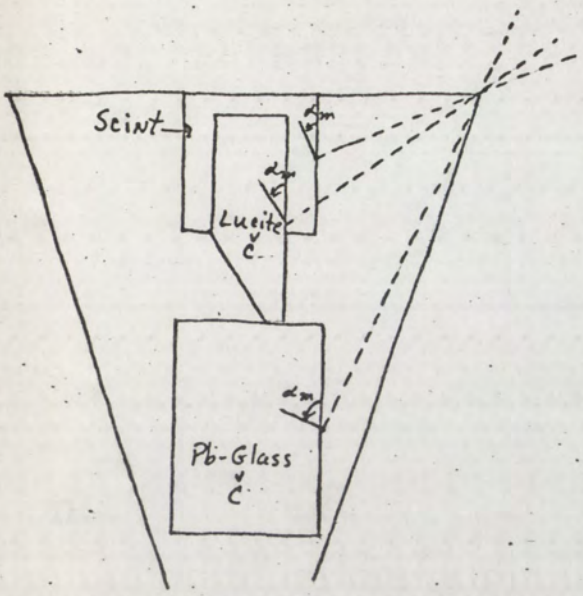

Scintillator: $\alpha_{min} \sim 30°$

Lucite C: $\alpha_{min} \sim 40°$

Pb-Glass C: $\alpha_{min} \sim 75°$

The angles subtended by the various particle trajectories must also be estimated since the threshold energy of the counters depends on α. To a very rough approximation the $2\alpha_{th}$ are twice α_{min} for each counter. Under this approximation the $eg(E,\alpha)$ contribution from the sides and top can be integrated over the same α values and then integrated separately over threshold energy.

The ratio of r(E) to J(E) is actually too large since it has been assumed that the flux strikes the counter from 0° to 2π in a given plane. This was modified to allow only particles striking the front or within 56° of the normal to either the top or bottom to be included in r(E).

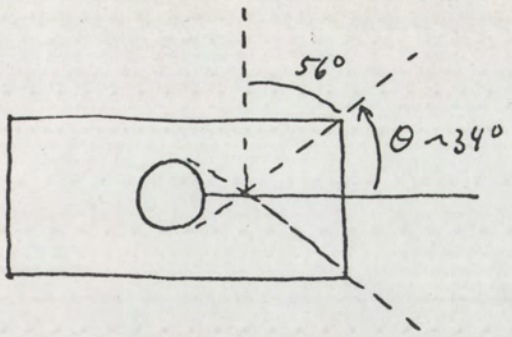

Front view

The fraction of the total intensity excluded is roughly:

$$4 \times 34^\circ = 136^\circ \sim \frac{3}{4}\pi \longrightarrow 3/8$$

$$eq(E,\alpha) = \frac{5}{4}\frac{a}{\pi}\left\{4h\,K(\alpha)\cos\alpha + \pi a \sin\alpha\right\} \quad cm^2$$

In integrating over α the elliptic integral $K(\alpha)$ was approximated by three linear functions:

$$K_3(\alpha) = 10.5\alpha - 10.98 \qquad \frac{5}{12}\pi < \alpha < \pi/2$$

$$K_2(\alpha) = 2.37\alpha - .33 \qquad \pi/3 < \alpha < \frac{5}{12}\pi$$

$$K_1(\alpha) = .89\alpha + 1.36 \qquad \pi/6 < \alpha < \pi/3$$

$$eq(E) = \frac{2}{\pi}\int_{\alpha_{min}}^{\pi/2} \frac{5}{4}\frac{a}{\pi}\left\{4h\,K(\alpha)\cos\alpha + \pi a \sin\alpha\right\} \frac{cm^2}{Mev}$$

Scintillator: $a = 7.6$ cm $h = 8.9$ cm

$$eq_s(E) = \frac{5}{2}\frac{a}{\pi^2}\left\{4h(.88) + \pi a(.866)\right\}$$

Lucite C: $a = 5.1$ cm $h = 9.9$ cm

$$eq_L(E) = \frac{5}{2}\frac{a}{\pi^2}\left\{4h(.81) + \pi a(.76)\right\}$$

Pb-glass C: $a = 10.2$ cm $h = 15.2$ cm

$$eq_{PbG}(E) = \frac{5}{2}\frac{a}{\pi^2}\left\{4h(.18) + \pi a(.26)\right\}$$

Appendix II

To obtain the total counting rate over all energies an energy spectrum of the form $f(E) = BE^{-N}$ was used. B is an unknown scale factor.

$$R = B\frac{5}{2}\frac{a}{\pi^2}\left\{\frac{4hA}{(N-1)}\frac{1}{E_{th(s)}^{n-1}} + \frac{\pi aC}{(n-1)}\frac{1}{E_{th(t)}^{n-1}}\right\}$$

A and C are the geometric factor coefficients for a particular counter and $E_{th(t)}$ and $E_{th(s)}$ are the thresholds for the counter top and sides.

For

$$J(>E_0) = B\int_{E_0}^{\infty} E^{-N}dE = \frac{B}{N-1}\frac{1}{E_0^{N-1}} \qquad \frac{\text{counts}}{\text{cm}^2\text{-sec}}$$

the conversion factor from experimental count rate to omnidirectional flux is

$$G = \frac{R}{J(>E_0)} = \frac{1}{4}aE_0^{n-1}\left[\frac{4hA}{E_{th(s)}^{n-1}} + \frac{\pi aC}{E_{th(t)}^{n-1}}\right] \text{cm}^2$$

When the total R is a mixture of protons and electrons the expression for G is not so simple in form since

$R_{tot} = R_p + R_e$. R_e can be determined from the Cerenkov counters and then subtracted from R_{tot} to estimate G for protons in the scintillator counting rate.